Newly Discovered Source of Turbulence and Heating in the Solar Chromosphere

Meers Oppenheim[1] ⬤, Yakov Dimant[1] ⬤, William Longley[1,2,3] ⬤, and Alex C. Fletcher[4] ⬤

[1] Center for Space Physics Boston University 725 Commonwealth Ave., Boston, MA 02461, USA; meerso@bu.edu
[2] Rice University Department of Physics and Astronomy Houston, TX, USA
[3] University Corporation for Atmospheric Research Boulder, CO, USA
[4] Naval Research Laboratories, Washington DC, USA

Abstract

Above the Sun's luminous photosphere lies the solar chromosphere, where the temperature increases from below 4000 K to over 1 million K. Though physicists do not understand the origin of these increases, they know it powers the solar wind with enormous consequences for the entire solar system. This report describes a set of simulations and analytical theory showing that solar atmospheric flows originating in the photosphere will frequently drive a previously unidentified thermal plasma instability that rapidly develops into turbulence. Though this turbulence is small scale (centimeters to a few meters), it will modify the conductivity, temperatures, and energy flows through much of the chromosphere. Incorporating the effects of this turbulence, and other small-scale turbulence, into large-scale models of solar and stellar atmospheres will improve physicists' ability to model energy flows with important consequences for the predicted temperatures and radiation patterns.

Unified Astronomy Thesaurus concepts: Solar chromosphere (1479); Quiet solar chromosphere (1986)

Supporting material: animation

1. Introduction

Over the last five decades, detailed spectral data combined with modeling have given solar scientists a clear picture of the average thermal structure of the quiet chromosphere (i.e., away from active regions such as sunspots; Athay 1966; Vernazza et al. 1981). Progressing upward from the photosphere, the temperature drops from 6000 K to below 4000 K at about 800 km, followed by a steep increase of a few thousand kelvin (see Figure 1). Above this, the temperature plateaus for another 2000 km before it spikes to over one million degrees kelvin in the transition region between the chromosphere and corona (Fontenla et al. 1993; Avrett & Loeser 2008). Though this upper temperature increase powers the solar wind, the lower temperature increase of a few thousand kelvin requires more energy because of the far higher gas densities there. Furthermore, the energy that reaches the transition region and powers the solar wind has to pass through the lower chromosphere. The importance of understanding energy flow through the chromosphere has motivated the space science community to deploy numerous space- and ground-based observatories and to engage in extensive modeling and simulation efforts (Pontieu et al. 2004; De Pontieu et al. 2014; Grant et al. 2018; Jeffrey et al. 2018; Liu et al. 2019).

Researchers have proposed and discarded a number of physical mechanisms to explain this lower heating region, including transient shock wave heating (Fossum & Carlsson 2005), nano-flares associated with magnetic reconnection (Aschwanden et al. 2000), Joule heating due to continuous dissipation of magnetohydrodynamic waves (Fontenla 2005), and anomalous heating associated with plasma turbulence (Fossum & Carlsson 2005; Fontenla et al. 2008, 2009; Hotta et al. 2019). Recently, our team and others have shown that Farley–Buneman (FB) waves should grow in this region and proposed this may explain the heating effect (Fontenla 2005; Fontenla et al. 2008, 2009; Gogoberidze et al. 2009; Madsen et al. 2014; Fletcher et al. 2018). However, when we ran fully

kinetic simulations of this system, we discovered that the excited waves have distinctly different characteristics from those generated by FB waves. This previous research had neglected electron and ion thermal effects, which we show here will dominate the wave growth. This paper presents these simulations and supporting analytical theory demonstrating the growth and propagation of these thermal waves. This paper also discusses the many potential consequences of the resulting turbulence, including chromospheric heating.

The chromosphere is an odd environment. The relatively low temperatures there cause a large majority of the hydrogen (H) to remain neutral, though some plasma exists. Chromospheric plasma is dominated by radiation created protons (H^+) and easily ionized heavy metals such as silicon (Si^+), magnesium (Mg^+), carbon (C^+), and iron (Fe^+) (Fontenla et al. 1993). Near the temperature minimum, the heaviest ions will often be demagnetized by collisions, meaning they no longer gyrate around the magnetic field and instead get dragged by neutral flows driven by photospheric convection. The still-magnetized electrons remain mostly tied to the field lines, thus neutral flows with a component perpendicular to B convert neutral flow energy into currents, making the system a dynamo (Dimant et al. 2016). If the electrons and neutrals drift relative to each other fast enough to exceed a threshold—that we calculate below—then the plasma becomes unstable to wave growth.

The source of the energy that heats the chromosphere remains an open question. In the quiet solar chromosphere, neutral flows contain far more energy than the magnetic field and therefore are a better candidate for providing energy to heat the chromosphere. At photospheric altitudes, both observations and simulations show average horizontal neutral gas flow speeds of around 2 km s^{-1} while chromospheric measurements show flows reaching nearly the neutral acoustic speed (5.5 km s^{-1}; Carlsson et al. 2007). This means that the ratio of the bulk-flow kinetic energy to thermal energy is between 0.1 and 0.5. This far exceeds the ratio of the magnetic to thermal energy density which lies between 0.018 and
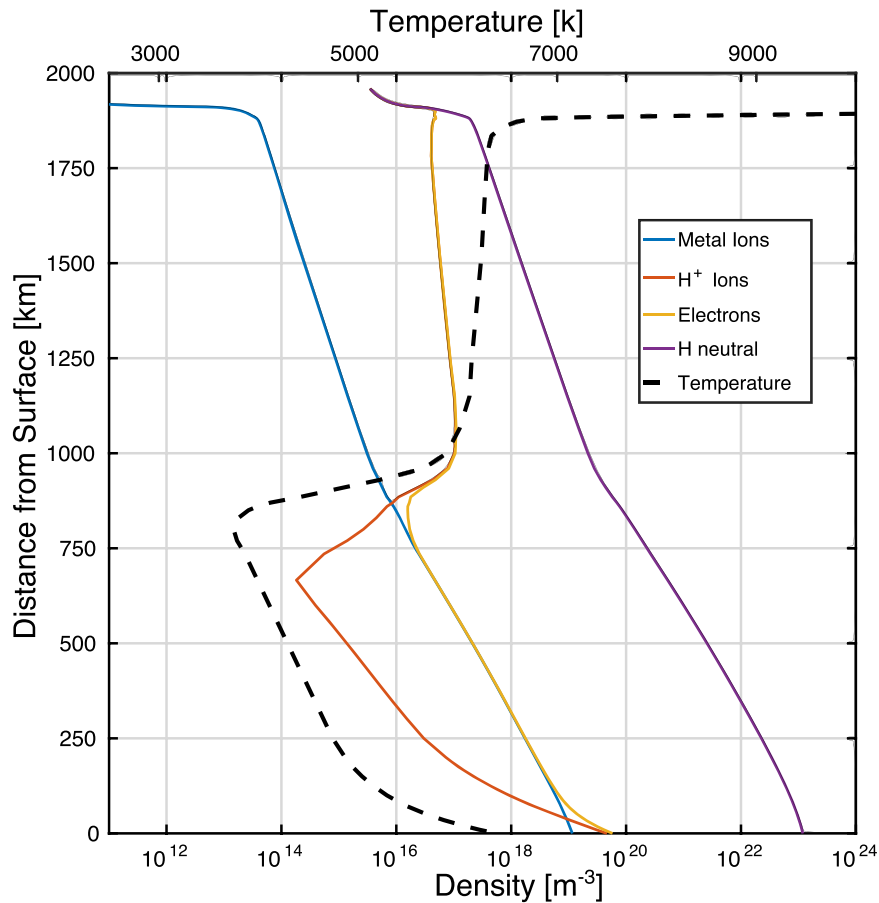
Figure 1. Density and temperature vary with distance from the solar surface. The dashed line shows the temperature (top axis) while the solid lines show various constituent densities. Note that the neutral H density exceeds the plasma density (electrons in yellow) and that the metals are the dominant species in the lower part of the chromosphere.

0.01. The heating mechanism we explore converts neutral flow energy into plasma wave energy, which then causes electron heating that could account for chromospheric observations.

The mechanism underlying this newly discovered thermal instability is related to the FB instability, which develops when magnetic fields cause electrons to drift in a different direction than the collisionally dominated ions. A similar thermal instability was discovered in the Earth's lower ionosphere, but there it plays only a minor role because the cooling effects of collisions with N_2 and O_2 are much larger than the cooling through collisions with H that dominates in the chromosphere (Dimant & Sudan 1995, 1997; Kagan & Kelley 2000; Dimant & Oppenheim 2004a; Oppenheim & Dimant 2004a). In the reference frame of a neutral gas flowing across the solar magnetic field $\boldsymbol{B}$, the electrons travel at roughly $\boldsymbol{u}_e \approx \boldsymbol{E} \times \boldsymbol{B}/B^2$, where the electric field results from the Lorentz transform of the B field into the frame moving at the neutral drift velocity $\boldsymbol{u}_n$ such that $\boldsymbol{E} = -\boldsymbol{u}_n \times \boldsymbol{B}$. As the electrons drift, they collide with neutrals, becoming hotter. If an acoustic-like compressional wave develops mostly in the plane perpendicular to $\boldsymbol{B}$, it will cause a local wave-induced electric field. This field will modify the electron drift speed and that will also modify the amount of heating, either increasing it if the electrons end up with a combined speed faster than $\boldsymbol{u}_e$, or reducing it otherwise. If the wave is oriented in a direction so that the heating is reduced on the wave crests, then the pressure term will draw more plasma into regions of already high density causing the wave to grow exponentially (Dimant & Oppenheim 2004b; Oppenheim & Dimant 2004b).

The system will naturally select waves with the highest growth rates and these waves will grow until nonlinear physics causes them to saturate, as seen in the following simulations.

This new instability mechanism heats the plasma and modifies energy flows in the coolest part of the chromosphere. In this region, conditions exist that will drive the thermal plasma instability at submeter to many kilometer scales. Since the fundamental timescale of the instability growth rate is microseconds, it will rapidly develop into plasma turbulence, heating the plasma. It will also transport electrons across the solar magnetic field, modifying the effective conductivities and, therefore, the current flows.

2. Simulation Results

To model the behavior of the chromosphere plasma we used a multispecies electrostatic particle-in-cell (PIC) plasma simulation that includes algorithms to accurately model collisions with neutral H (HI) particles. This captures the full kinetic physics down to the Debye length (submillimeter) and as rapidly as the electron gyrofrequency (hundreds of megahertz). This, of course, limits the total scale of the simulations to a few meters in total size and a few milliseconds. Nevertheless, these allow us to resolve both wave growth and the development of turbulence in 2D. We perform these simulations in the HI frame of reference where the static magnetic field, $B\hat{z}$, lies perpendicular to the plane of the simulations ($\hat{x}, \hat{y}$). In this frame of reference an
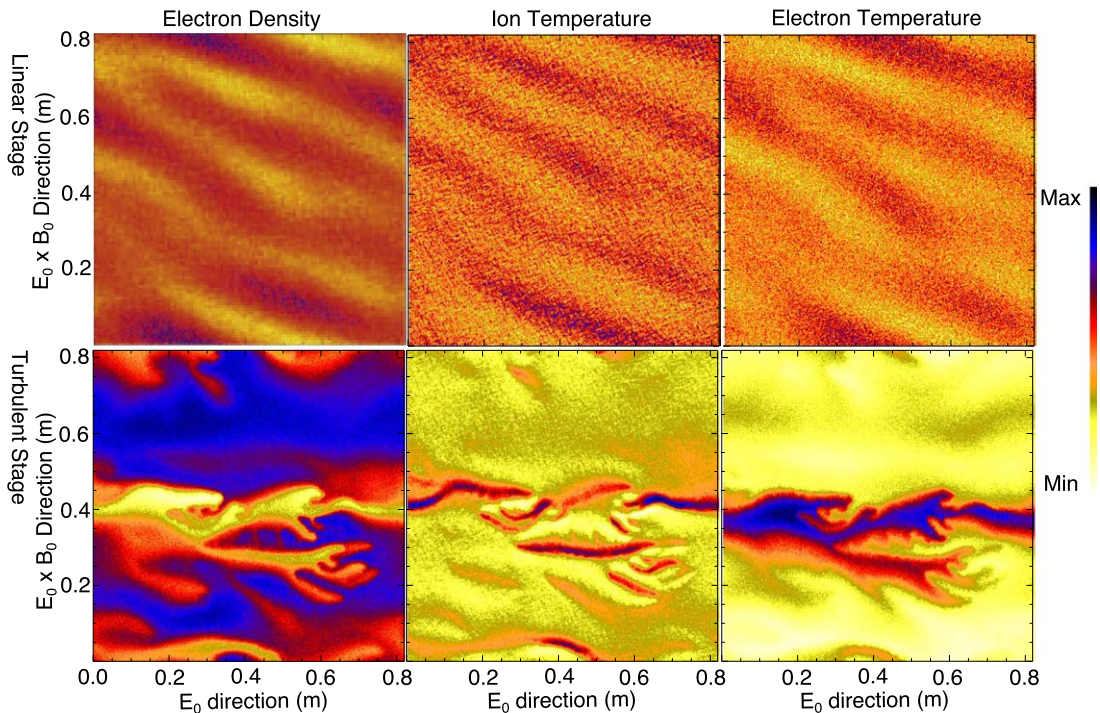
Figure 2. Compares electron density perturbations (left), ion temperature (center), and electron temperature (right) during the linear growth stage (top) and in saturation (bottom) from the 2D PIC simulation. The animation tracks the electron density only. The run parameters imitated conditions at the temperature minimum where the H+ density roughly equals the combined densities of all the metal ions. The drift speed of electrons in the frame of the neutrals is 9.1 km s^{-1} while the H ion acoustic speed is 7.9 km s^{-1}.

(An animation of the first column of this figure is available.)

externally imposed electric field E points in the $\hat{x}$ direction causing electrons to mostly drift downward ($-\hat{y}$) due to a $E \times B$ motion but with a small collisional Pedersen drift in the $-\hat{x}$ direction. These simulations only model collisions between the charged species and HI. Since the HI density exceeds the electron density by at least 3 orders of magnitude, the code assumes that the HI velocities and temperatures do not change. Also, these simulations do not last long enough for ionization and recombination to play an important role and therefore ignores these effects. Appendices A and C include more detailed descriptions of the algorithms and a full list of the parameters.

A number of features of the waves during the linear growth stage reveal that thermal instabilities dominate the physics of this system. Figure 2 (top) shows the electron density and electron and ion temperatures as functions of position in the simulation. First, the orientation of the wave fronts points at a 33° angle from the $E \times B$ direction ($+\hat{x}$), something predicted by the linear theory of electron thermal waves. Second, the phase angle between the electron density perturbations and electron temperature is close to 90°. Third, the dominant wavelength is about 19 cm, close to that predicted for the thermal instability but over 35 times the length expected for the FB instability. The FB instability does not generate these characteristics but the thermal instability does, as discussed in the analysis section.

Figure 2 (bottom) shows the turbulent nature of the saturated thermal instability (see the animation). This results from wave–wave coupling, feeding energy from the growing modes into dissipative modes. This process can be modeled statistically to give average consequences of the saturated turbulence (Dimant & Milikh 2003). The animated version of Figure 2 shows the
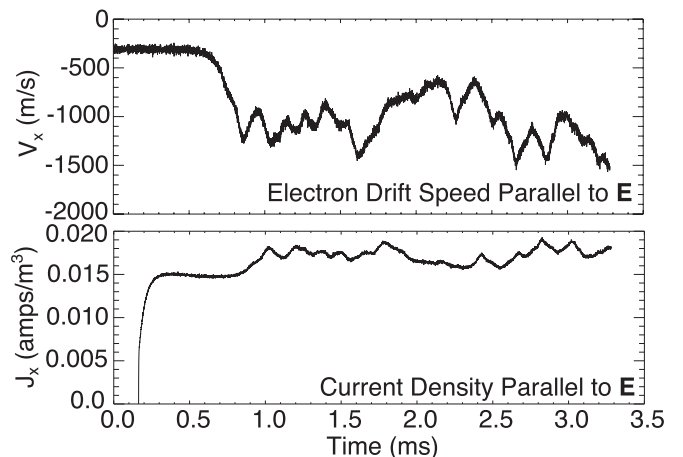

Figure 3. Top image shows the net electron drift speed across B in the E direction, starting with the small, cross-field Pedersen drift rate of -350 m s^{-1} and then more than tripling to an average of around -1050 m s^{-1}. The lower image shows the resulting net current density in the same direction, showing an increase of around ~16%.

transition from linear to nonlinear dynamics by following the evolution of the electron density.

The simulations show that thermal instability-driven turbulence causes anomalous cross-B-field transport, meaning that it will modify the conductivity of the plasma. Figure 3 shows the effect in our simulations. Though the electron drift speed across the externally imposed E-field increases dramatically, the current only increases modestly because the ions carry most of the current in this direction. The magnitude of this anomalous
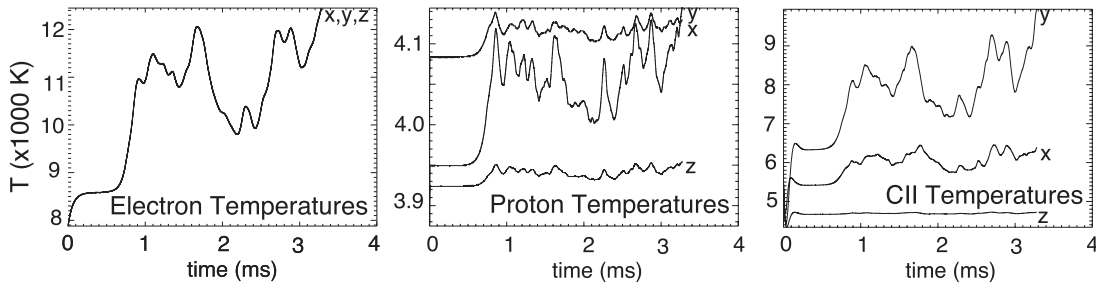
Figure 4. Simulation predicted temperatures for the electrons, protons, and the hottest metals, C^+. The temperature is calculated by taking the first moment of each particle distribution in each direction (labeled x, y, and z). The initial temperature at $t = 0$ was an estimated temperature for each species due to its drift speed through the neutrals. The plateau seen from 0.1–0.6 ms results from the simulation calculating the actual temperature resulting from Joule heating due to the static electric field. Then the increase that occurs immediately after that results from the growth in the waves and the final temperature is set by the saturated instability.

current may change dramatically for different solar conditions or altitudes. This cross-field transport develops because the small-scale electric field generated by the waves causes (δE) the electrons to $\delta E \times B$ drift across B in the direction of the large-scale driving E field. While the $\delta E \times B$ motions go both along and against E, Figure 3 shows that more electrons travel in the direction to enhance the Pedersen current than to reduce it. Effectively, this anomalous current works to short out its driver and we expect this will happen in much of the mid-chromosphere (Oppenheim 1997; Oppenheim & Dimant 2013).

2.1. Heating

Small-scale turbulence can lead to dramatic electron heating in the FB system in the ionosphere, and this similar turbulence will contribute to chromospheric electron heating that, in-turn, can lead to the spectral measurements we observe (Foster & Erickson 2000; Milikh & Dimant 2003; Oppenheim & Dimant 2013). These simulations show heating as illustrated by Figure 4. In order to obtain a sufficiently long run and to emphasize heating, this figure shows a simulation of half the size in both directions and double the driving electron drift rate. The temperature of the plasma initially matches the neutrals at 3800 K but the plasma temperature quickly rises to higher levels, to over 11,000 K for the electrons, a temperature at which the electrons will interact with the neutral metals and cause radiation.

The heating results from charged particles colliding with the neutrals, converting drift energy—which ultimately derives from neutral flows and magnetic field energies—into heat. Each component of the plasma heats to a different level as the combined effects of the electric and magnetic fields cause them to drift with respect the to the neutral gas atoms. In the frame of reference of the neutrals, the fields cause the plasma species to drift with respect to the neutrals. The simulations work in this frame of reference. This heating is balanced by the cooling effect of colliding with a 3800 K neutral hydrogen (HI) gas. In these simulations, the HI gas does not respond to the changes in the plasma, maintaining a constant velocity and temperature. For the short duration of these simulations, this is a reasonable assumption, on longer timescales, we would expect that the HI would evolve due to collisions with the plasma.

The initial heating from 0 to 0.6 ms results just from the drift motions caused by $E_0 \times B_0$ and the collision rates. Using a relatively simple fluid analysis, Equation (9) predicts the expected magnitude of this heating. The baseline simulation starts each species at the temperature predicted by this equation

and the simulator shows the temperature rising a small amount from this level in this period as the distribution function distorts, physics neglected by Equation (9). The protons show the least heating, presumably because they have the highest collision rates and lowest drift rates while the C+ has the most of any of the metals, being the lightest and therefore most magnetized.

Figure 4 also shows that the heavier plasma species deviate from isotropic. The light electrons scatter rapidly, maintaining equal temperatures in all directions. However, collisions elevate metal ion temperatures in the $E_0 \times B_0$ drift direction $\hat{x}$ more than in the Pederson drift direction $\hat{y}$ while the B direction $\hat{z}$ is only slightly warmed.

Once the turbulence begins, the temperatures shoot up again, a result of the turbulence-generated electric fields, with each species heating a different amount. The electrons clearly show the most heating, first rising 125% during the laminar flow stage (before the turbulence develops) and then rising another 125% due to the turbulence. The protons only increase on the order of 5% initially and a bit more in response to the turbulent fields. The C II increases by 70% due to laminar flow in the $\hat{x}$ direction but by just under double this due to turbulence to 125%. The other metals behaved similarly to the C II but reaching smaller maximum amplitudes (Fe II $\Rightarrow$ 80%, Mg II and Si II by about 100%). These simulations may substantially underestimate electron heating because they are small in size and neglect the third dimension (Oppenheim & Dimant 2013). The third dimension plays a primary role in FB heating in the ionosphere because the waves cause small electric fields to develop along B and this accelerates electrons that collide with neutrals and heat intensively. This may happen in the chromosphere as well.

3. Linear Theory

An analysis of the thermal instability allows us to predict where and under what conditions in the chromosphere waves will grow. This can be done by assuming fluid equations for the conservation of mass, momentum, and energy appropriate for each species in the chromosphere. Those, plus the assumption of quasineutrality, enable one to convert these equations into a dispersion relation that predicts conditions that will lead to wave growth and propagation. Appendix D presents the results of this derivation and discusses the numerical techniques used to solve them.

Solutions of the linear dispersion Equation (10) give the criterion necessary to generate thermal instabilities and the
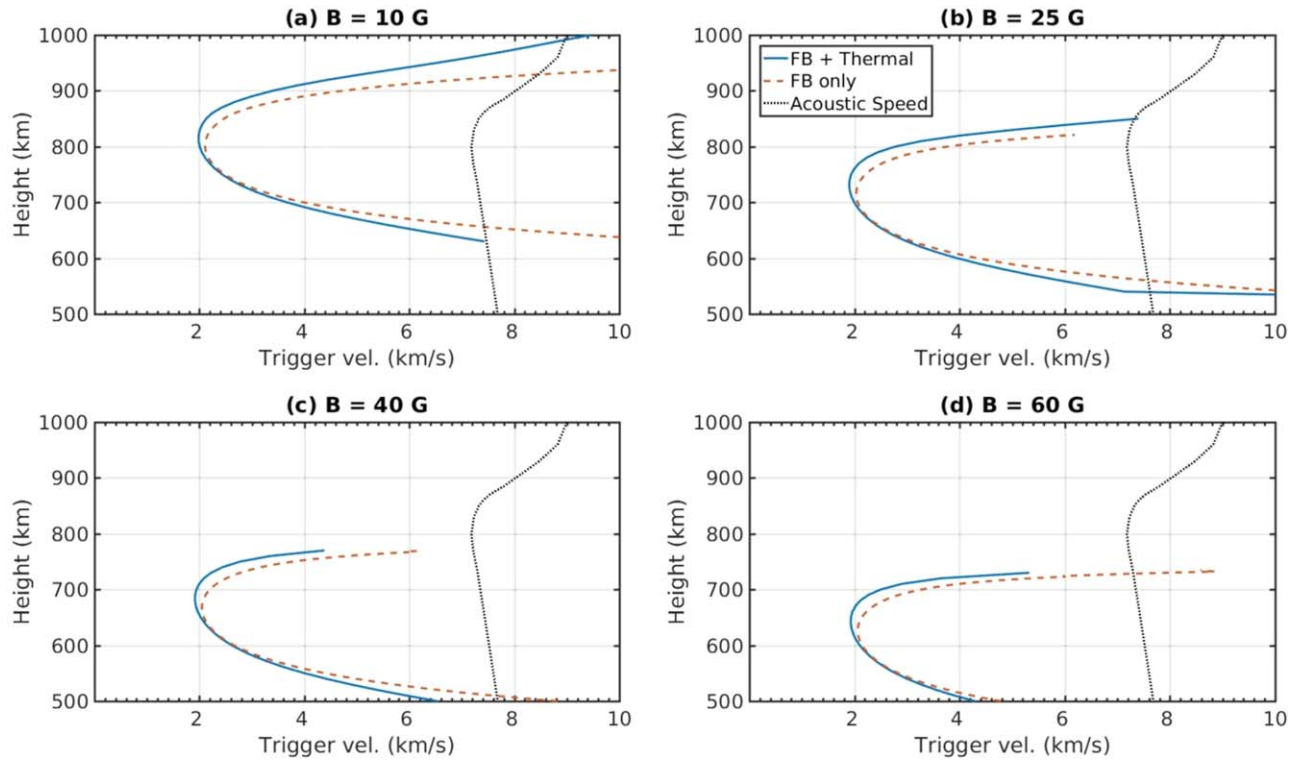
Figure 5. Predicted altitude range of instabilities for a range of magnetic field strengths. The trigger velocity is the minimum difference between the electrons and neutral speeds perpendicular to B needed to drive the instability. The "FB + Thermal" line derives from the full thermal instability (which includes Farley–Buneman (FB) effects). The solid line shows the sound speed for neutral H.

subsequent turbulence. Figure 5 shows the velocity difference between the electron drifts and neutral flows needed to trigger the instability for a range of magnetic fields. It shows that, even at a fraction of the neutral hydrogen sound speed, these waves will grow over a broad range of chromospheric altitudes. This uses compositions and temperatures from semiempirical nonthermal equilibrium radiative transport models (Fontenla et al. 2009). These models yield an average set of conditions for the quiet Sun. The figure shows that at all heights the thermal instability has a lower threshold than the FB instability. It also shows how the trigger speed depends strongly on the magnetic field, something that should have substantial observational consequences. Once researchers have a better ability to measure the magnetic field of the quiet Sun, then a comparison of temperatures to field strength should determine how much this heats the chromosphere (Rubio & Suárez 2019).

4. Chromospheric Modeling

Combining a model of the solar atmosphere with our dispersion relation enables us to estimate where the conditions necessary to create the thermal instability exist. For this, we used output from the Bifrost model of the solar atmosphere described in Martínez-Sykora et al. (2017a), Martínez-Sykora et al. (2017b), and Gudiksen et al. (2011) to obtain the electric fields and pressures. We then use the model described in Fontenla et al. (2009) to determine the species fractions. Combining all this information, we apply the instability criterion for the FB instability. Figure 6 shows regions where we predict the FB instability will develop with the lighter

areas showing where the instability far exceeds the threshold and we would expect large-scale heating. While it would be better to apply the full dispersion relation for the thermal instability described in Appendix D, we have not yet been able to solve it quickly over such a large range of parameters. The thermal instability is easier to trigger than the FB instability, meaning that this figure underestimates how unstable the chromosphere is to this class of small-scale instabilities. We want to note that this type of calculation is not fully self-consistent as the Bifrost simulator assumes a single plasma species and neglects other components important in a highly collisional plasma.

Bifrost cannot model the physics underlying thermal or FB instabilities even when including Hall and ambipolar diffusion terms discussed in Martínez-Sykora et al. (2017a, see Equation (1)). Both the PIC code and the fluid theory we discuss in the appendices include a number of additional factors neglected by BiFrost's underlying equations but playing an important role for our small-scale instabilities (Gudiksen et al. 2011; Martínez-Sykora et al. 2017a, 2012, 2017b). First, BiFrost's solves a system of equations that assume only one species of ion and neutrals, while multi-ion species, each responding to the magnetic field differently, play an important role in thermal waves. Second, we include the ion inertia, essential in the FB instability, while BiFrost only tracks the combined ion and neutral inertia. Third, BiFrost neglects plasma pressure gradients, which play a central role in thermal instabilities. Lastly, BiFrost treats the neutral species as part of the dynamic fluid, while we perform our local computations assuming a uniform neutral flow, unperturbed by the plasma.
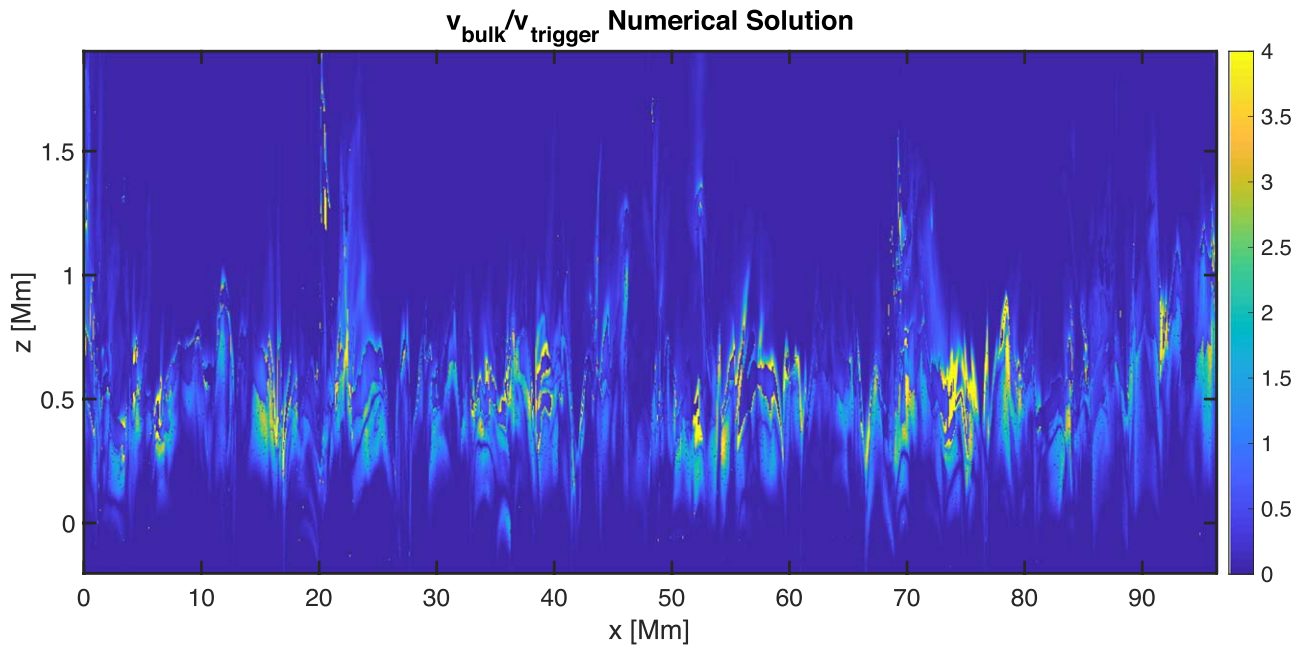
$v_{bulk}/v_{trigger}$ Numerical Solution

Figure 6. Ratio of electron drift velocity to the velocity necessary to trigger the FB using data from a BiFrost simulation.

5. Discussion and Conclusions

The simulations presented show that thermal instabilities easily generate meter-scale turbulence and waves. The linear theory supports this and also predicts the chromospheric conditions most conducive to the generation of these waves. These waves will have important consequences for energy flows and conductivities throughout the chromosphere.

The linear form of these equations yields a set of growth rate and wavelength predictions. Figure 9 in Appendix D shows the growth rate as a function of wavelength predictions for the parameters used in the simulation, showing that electron thermal instabilities grow at the predicted wavelengths. These equations also demonstrate that the threshold neutral wind or electric field necessary to drive a pure FB instability is considerably higher and, therefore, the thermal instability grows first and dominates the wave growth and ultimately, the nonlinear behavior of the system. Nevertheless, the FB component still contributes.

The dominant centimeter- to meter-scale sizes of chromospheric thermal waves make them difficult to directly detect. However, there is the possibility of using radio sounding techniques to measure them, since they create copious density irregularities in the range of wavelengths frequently used by radars. Also, the prediction that the altitude where thermal instabilities develop depends strongly on the magnetic field strength and direction should enable observers to detect their consequences by mapping heating as a function of magnetic field strength.

One important consequence of this turbulence is the transport of electrons across the magnetic field. Without the waves, the electrons can only slowly Pederson drift across B due to their collisions with neutrals. The turbulence carries them across B by creating a perturbed electric field that $E \times B$ transports them. This helps short out the driving field and should be modeled as anomalous conductivity. Such cross-field transport is of substantial consequence in many plasmas but can be included as a modified parameter in large-scale simulation (Liu et al. 2016).

While we have shown that these waves will be abundant, assuming the conditions predicted by the Bifrost simulator are approximately correct, their role in the heating and dynamics of the chromosphere remain an open question. In the Earth's atmosphere researchers have known for decades that small-scale waves play crucial roles in generating the large-scale structure. If this example holds, then solar physicists will need to incorporate this and, presumably, other sources of small-scale waves in order to create accurate models of the solar atmosphere and ultimately understand the physical mechanisms responsible for solar heating.

Appendix A
Chromospheric Collisions and Parameters

Collisions in the solar chromosphere are complex, though cross-sections for the most common collisions, e^-–H and H^+–H, have been calculated and measured in the laboratory in the appropriate energy range (Vranjes & Krstic 2013). However, the metal-H collision rates have proven more challenging to obtain. One must include a number of collision types: momentum transfer, resonant charge exchange between H and H^+, and Coulomb collisions between electrons and ions (but not intraspecies Coulomb collisions because they do not affect bulk velocities or temperatures). The collision frequency used in the simulations and the linear theory were approximated by the sum of these three collision frequencies.

In the chromosphere, the relatively low energies means that the dominant collision mechanism between charged particles and the neutral hydrogen (HI) are an elastic Maxwell molecule collision where the charged particle causes the neutral species to polarize as it approaches. This assumption leads to the classical
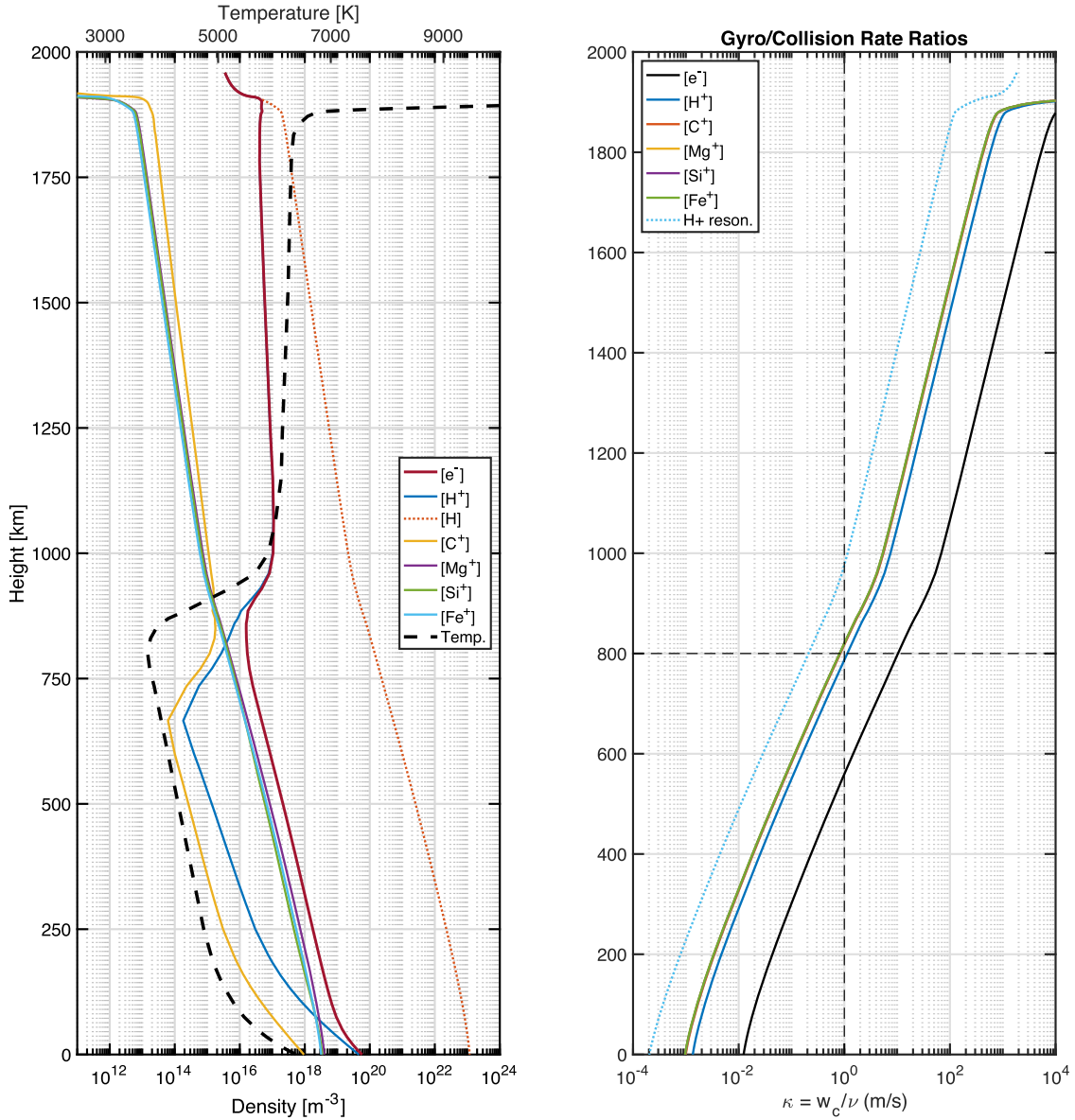
Figure 7. Temperature and density vs. height above photosphere (left) and the ratio of the gyrofrequency to collision frequency vs. height (right). The right image shows lines for two H+ collision rates but the dotted line represents a better model of collision rates that includes resonant charge exchange.

model of collisions between charged species and neutrals of

$$\nu_{sn} = 2.21 \pi n_n \frac{m_n}{m_s + m_n} \sqrt{\frac{\alpha_n e^2}{4 \pi \epsilon_0 \mu_{sn}}} \qquad (1)$$

$$= 1.96 n_n \sqrt{\frac{\alpha_n e^2 m_n}{\epsilon_0 m_i (m_i + m_n)}}, \qquad (2)$$

where n_n is the neutral H number density, α_n is the polarizability, m_s is the species mass, μ_{sn} is the reduced mass, and ϵ_0 is the vacuum permittivity (Dalgarno et al. 1958; Schunk et al. 2009; Vranjes & Krstic 2013). The polarizability of neutral hydrogen is $\alpha_H = 0.67 \times 10^{-24}$. Maxwell molecule rates are independant of velocity.

For $H^+ - H$ collisions resonant charge exchange increases the collision rate such that

$$\nu_{res} = 2.65 \cdot 10^{-16} n_H \sqrt{T_{H*}} (1 - 0.083 \log_{10} T_{H*})^2, \qquad (3)$$

where n_H is the number density of neutral hydrogen (in m^{-3}) and T_{H*} is the average temperature of H and H^+. For Coulomb collisions, the average collision frequency with the Spitzer correction is

$$\nu_{je} = \frac{m_e \pi n_e e^4 \ln(12 \pi n_e \lambda_D^3)}{m_s (4 \pi \epsilon_0)^2 \sqrt{m_s (2 k_b T)^3}}, \qquad (4)$$

where the Debye length, λ_D, is given by

$$\lambda_D = \sqrt{\frac{\epsilon_0 / e^2}{n_e / k_b T_e + \sum_j Z_j^2 n_j / k_b T_j}}, \qquad (5)$$

where Z_j is the charge state of the jth ion.

Figure 7 shows the ratio of cyclotron frequency to the sum of these collision frequencies for $B = 25$ G. At the temperature minimum and heating regions, it can be seen that the electrons have $\Omega_e \gg \nu_e$ (magnetized), the protons have $\Omega_p \ll \nu_p$ (demagnetized), and the metals have $\Omega_s \sim \nu_s$. In regions of

higher magnetic field the curves will all shift rightward making all the species more magnetized. This figure corrects an error in metal collision rates in Madsen et al. (2014) and Fletcher et al. (2018) which dropped a factor of the electron to ion mass ratio.

Appendix B
Assumptions of Fluid Model

This theory assumes a static $\boldsymbol{B}$, meaning it applies only to temporal and spatial scales shorter than that at which $\boldsymbol{B}$ changes in the chromosphere. It also assumes a multispecies, partially magnetized, quasineutral fluid plasma colliding with a far denser neutral gas. Assuming mass, momentum, and energy conservation, the governing equations are:

$$\frac{\partial n_s}{\partial t} + \nabla \cdot (n_s \boldsymbol{V}_s) = 0 \tag{6}$$

$$m_s \left(\frac{\partial}{\partial t} + \boldsymbol{V}_s \cdot \nabla \right) \boldsymbol{V}_s = q_s (\boldsymbol{E} + \boldsymbol{V}_s \times \boldsymbol{B})$$
$$- \frac{\nabla (n_s T_s)}{n_s} - m_s \nu_s \boldsymbol{V}_s \tag{7}$$

$$n_s^{2/3} \left(\frac{\partial}{\partial t} + \boldsymbol{V}_s \cdot \nabla \right) \left(\frac{T_s}{n_s^{2/3}} \right) = \frac{2}{3} M_s \nu_s V_s^2 - \delta_s \nu_s (T_s - T_n), \tag{8}$$

where n_s, m_s, V_s, T_s, and ν_s are the density, atomic mass, average fluid velocity, temperature, and collision rate with H of each species labeled with s. This applies to electrons as well as all the ion species, though the electron mass is sufficiently small that the electron inertia can generally be neglected. Also, $\delta_s = 2m_s/(m_s + m_n)$ where m_n is the atomic mass of the neutral species (mostly, H) and $M_s \equiv m_s m_n/(m_s + m_n)$ is the reduced mass of each species. Heat conductivity and viscosity play no role within the temporal and spatial scale of this instability and are not included in these equations. These equations apply in the frame of reference of the neutral gas, though it is easy to adapt them to other frames. These, combined with quasineutrality, govern the plasma dynamics of the system this paper explores.

Appendix C
Simulation Details

These simulations were performed with EPPIC, our massively parallel electrostatic PIC code (Oppenheim & Dimant 2004b, 2013). This code simulates the fully kinetic behavior of both electrons and ions using many of the standard techniques (Birdsall & Langdon 1985). This accurately and self-consistently models all plasma dynamics, including thermal effects, at the cost of substantial computer time. In addition, we implement a fairly novel algorithm that optimizes these codes for modern parallel supercomputers and allows us to use up to 10^{10} particles on grids up to 1024^3 in size (Oppenheim et al. 2008).

The EPPIC code has numerical routines for electron-neutral (e^--n) and ion-neutral (i^+-n) collisions which are crucial in both the lower ionosphere and chromosphere. The collisional algorithm has been designed to properly describe *elastic* collisions with both the appropriate rate of momentum and energy loss (Gurevich 1978; Schunk et al. 2009). EPPIC implements a number of charged-neutral collision algorithms, including a hard-sphere elastic model where the likelihood of

collision is linearly proportional to the macroparticle's velocity relative to a neutral particle (i.e., a constant cross-section) and a Maxwell molecule (constant collision rate) model. These techniques yield average Hall and Pedersen drift rates and particle heating and cooling rates predicted by laminar fluid theory. We can modify the mass of the neutral and/or the collision rate to mimic inelastic collision processes (Oppenheim & Dimant 2004a), making it velocity dependent.

EPPIC applies a novel approach to running on massively parallel computers. First, it divides the spatial region into many computational domains, so that each processor contains a small subset of the entire mesh. Second, within each domain, it subdivides the particles within that domain among a set of processors. For instance, to perform a 4096 × 4096 simulation, we divide the simulation region into 32 domains and then further divide the particle population in each domain among 32 processors, efficiently using 1024 cores. By varying the number of domains and the number of processors working on the particles in each domain, we can efficiently use a few hundred to tens of thousands of processors simultaneously, producing the same results as would a single processor but in a fraction of the wall-clock time. To implement this technique we utilize many parallel technologies, including a multiprocessor, spectral Poisson's equation solver to calculate the electric fields, and message-passing libraries to pass particles and boundary cells between neighboring processors. All this has been completed and extensively tested (Oppenheim & Dimant 2013; Longley et al. 2019).

The simulations revealed that one needs all three Equations (6)–(8) to model the solar chromosphere as a fluid, and that thermal waves dominate wave growth. For pure FB waves, Equation (8) is replaced by an isothermal or adiabatic equation of state. In thermal waves, the heating and cooling modeled by the two terms on the right-hand side of the thermal Equation (8) play a central role.

Linear fluid theory enables us to evaluate the conditions required to trigger the development of these waves and therefore to estimate the regions of the solar atmosphere where they will develop. The simulations provide a double check on the linear theory and also allow one to probe the nonlinear evolution of the waves and their subsequent heating effects.

This paper compares all simulations to a baseline case run with parameters specified in Table 1. These parameters reproduce the physics of the quiet-Sun chromosphere under typical conditions. A number of comparison runs were done to evaluate the range of parameters over which this system would develop.

The simulation parameters derive from the semiempirical quiet-Sun model (Fontenla et al. 2009). Because the simulator needs to resolve the Debye length, we reduce the plasma density by a factor of 1000. This should not affect the results substantially since the density does not appear in the linear dispersion relationship (Equation (10)). Even in the nonlinear fluid equations, the density only appears in the form of $\nabla n/n = \nabla (\ln n)$ and, therefore, it depends weakly on the absolute value of the density. We tested this by running with up to 10x larger densities, though this required a smaller simulation box. Nevertheless, the effects of the absolute value of the density needs to be more fully explored.

The coefficient n_{sv} indicates the number of PIC particles representing the physics of species s. This number is scaled by
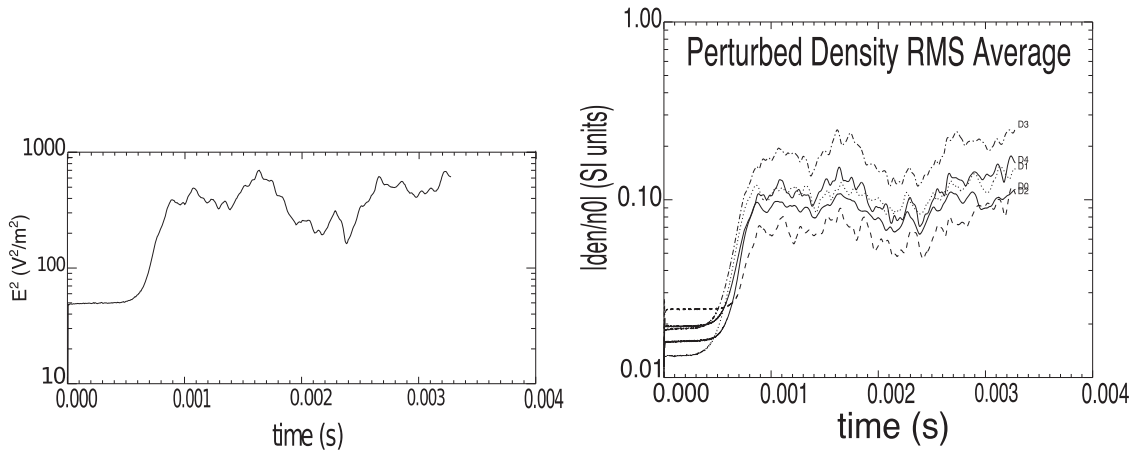
Figure 8. Globally averaged electric field squared (left) and rms densities (right) from the baseline simulation.

the density number, n_s, and does not impact the effective density but does impact the noise in the simulation.

The baseline case evolves density and temperatures starting from noise. The particle density sets the level of this noise. By tracking the total energy in the electric field throughout the simulation, one can see how far above the noise the wave's energy develops, as seen in Figure 8. The simulation noise, seen before $t = 0.5$ ms, is about $\langle E_{noise}^2 \rangle \approx 50$ (V m^{-1})^2 while the average level after saturation, while quite variable, is $\langle E^2 \rangle \approx 400$ (V m^{-1})^2, meaning the noise level is just above 10%. One would expect that this level of noise could impact the nature of the turbulence only a small amount.

The globally averaged rms densities also reveal how far above the noise level the waves of each species reach at saturation. Figure 8 shows this evolution. It also makes clear that all the species develop waves.

These waves are a chromospheric form of thermal plasma waves initially described for the ionosphere (Dimant & Oppenheim 2004b; Oppenheim & Dimant 2004b). Based on those theoretical predictions, Gogoberidze et al. (2014) speculated that the electron thermal instability may play a role in the chromosphere while ion thermal effects have little impact. The simulation results demonstrate that electron thermal waves not only play a role, but dominate the instability mechanisms. Figure 2 of the main article shows the relative phase between the density and temperatures, and indicates the nature of the instability as well as the characteristics mentioned above.

Figure 5 of the main article compares the linear theory predictions for instability growth rates γ of pure FB waves with combined thermal + FB waves. This shows that for these parameters, FB waves should not grow ($\gamma < 0$). It does show that the combined instability will grow at 45° from the $\boldsymbol{E} \times \boldsymbol{B}$ drift direction. It also predicts a peak growth rate at a wavelength of ~ 0.23 m, very close to that seen in the top images of Figure 2 of the main article. Both the simulations and linear theory strongly points to a thermal instability mechanism.

Small-scale turbulence can lead to dramatic plasma heating, and this may contribute to measured solar atmospheric temperatures. These simulations show just such a heating effect as illustrated in Figure 4 of the article. The temperature of the neutrals initially starts at 3800 K but the plasma temperature quickly rises to higher levels due to collisions

between the drifting plasma species and the neutrals. Each species heats to different levels as electric fields cause them to drift at different speeds with respect to the neutral gas. In the frame of reference of the magnetic field, one would argue that magnetization causes the plasma species to drift with respect to the neutrals. However, these simulations work in the frame of reference of the neutral gas where an electric field drives these drifts. In either reference frame, the heating results from these plasma particles colliding with the neutrals. This heating is balanced by the cooling effect of colliding with a 3800 K neutral H gas.

The initial heating from 0 to 0.7 ms results just from the drift motions caused by $\boldsymbol{E}_0$, $\boldsymbol{B}_0$ and the ν_s. Equation (8) predicts the expected magnitude of this heating by assuming steady state drifts,

$$T_{s0} = T_n + \frac{2M_s \nu_s V_s^2}{3\delta_s \nu_s} = T_n + \frac{2M_s \kappa_s^2 V_0^2}{3\delta_s(1 + \kappa_s^2)}, \qquad (9)$$

where $\kappa_s \equiv |q_s| \, B/(m_s \nu_s)$. The baseline simulation started each species at the temperature predicted by this equation and the simulator shows the temperature rising a small amount from this level in this period. The reason this does not exactly match the Equation (9) temperature is this analysis neglects distortions in the distribution function while the simulator captures this. The protons show the least heating, because they have the lowest drift rates and collisions resulting from charge exchange. The C$^+$ has the most of any of the metals, being the lightest and most magnetized.

This figure also shows that the heavier plasma species deviate from isotropic. The light electrons collide rapidly maintaining equal temperatures in all directions. However, collisions elevate metal temperatures in the $\boldsymbol{E} \times \boldsymbol{B}$ drift direction ($\hat{x}$) more than in the pedersen drift direction ($\hat{y}$) while the $\boldsymbol{B}$ direction ($\hat{z}$) is only slightly warmed.

Once the turbulence begins, the temperatures shoot up again, a result of the turbulence-generated electric fields, with each species heating a different amount. The electrons clearly show the most heating, first rising 125% during the laminar flow stage (before the turbulence develops) and then rising another $\sim 125\%$ due to the turbulence. The protons only increase on order of 5% initially and a bit more in response to the turbulent fields. The C II increases by $\sim 70\%$ due to laminar flow in the $\hat{x}$

direction but by just under double this due to turbulence to ∼125%. The other metals behaved similarly to the C II but reaching smaller maximum amplitudes (Fe ∼ 80%, Mg II and Si II ∼ 100%).

Overall, the heating effect demonstrated by these simulations can play a role in heating the solar atmosphere. However, because these simulations neglect the third dimension and are small in size, they almost certainly substantially underestimate this heating.

Appendix D
Linear Multi-fluid Theory

This linear theory builds on earlier theories (Madsen et al. 2014; Fletcher et al. 2018) but adds in the neglected thermal terms. This improved linear theory provides a dispersion relation that predicts wave growth. This section will also compare the resulting growth predictions to simulation growth rates.

Starting with Equations (6)–(8), assuming quasineutrality $\nabla \cdot \boldsymbol{J} = 0$, dropping electron inertia and nonlinear terms, and then assuming linear plane waves and highly magnetized electrons $\kappa_e \gg 1$, these equations simplify to yield a combined FB and thermal dispersion relation of

$$1 + \sum_j \frac{\rho_j \alpha_j A_j}{A_e} \left(\frac{1 - (1 + 2/(3\mu_e)A_e - B_e/\mu_e}{1 - (1 + 2/(3\mu_i)A_j - B_j/\mu_j} \right) = 0 \quad (10)$$

where the variables are defined as follows: ρ_j is the fraction of a given ion species j; $\alpha_j \equiv T_{e0}/T_{j0}$ as defined by Equation (9); and

$$\mu_e = 1 + \frac{i\delta_e \nu_e}{\omega_{ke}}, \qquad \delta_e \approx \frac{2m_e}{m_n}$$
$$\mu_j = 1 + \frac{i\delta_j \nu_j}{\omega_{kj}}, \qquad \delta_j = \frac{2m_j}{m_j + m_n} . \quad (11)$$

This assumes elastic collisions, $m_n \approx m_p$. Further,

$$\omega_{kj} \equiv \omega - \boldsymbol{k} \cdot \boldsymbol{V}_j, \qquad \omega_{ke} \equiv \omega - \boldsymbol{k} \cdot \boldsymbol{V}_0 \quad (12)$$

where ω_{ks} are the Doppler shifted frequencies in which $\omega = \omega_r + i\gamma$ is the complex frequency. The zeroth-order mean fluid velocities of a particle s are given by

$$\boldsymbol{V}_s = \frac{\frac{q_s \boldsymbol{E}_0}{m_s \nu_s} + \frac{q_s^2 B^2}{m_s^2 \nu_s^2}\boldsymbol{V}_0}{1 + \frac{q_s^2 B^2}{m_s^2 \nu_s^2}} = \left(\frac{q_s \boldsymbol{E}_0}{m_s \nu_s} + \kappa_s^2 \boldsymbol{V}_0 \right) \Big/ (1 + \kappa_s^2) \quad (13)$$

where $\boldsymbol{V}_0 \equiv (\boldsymbol{E}_0 \times \boldsymbol{B})/B^2$ is the $\boldsymbol{E}_0 \times \boldsymbol{B}$ drift velocity and $\kappa_s = |q_s| B/(m_s \nu_s)$; for ions $q_j = e$, for electrons $q_e = -e$.

For all electron and ion species

$$A_s = -i \frac{V_{Ts}^2}{\nu_s \omega_{ks}} \left(\frac{(1 - i\omega_{ks}/\nu_s)k_\perp^2}{\kappa_s^2 + (1 - i\omega_{ks}/\nu_s)^2} + \frac{k_\parallel^2}{1 - i\omega_{ks}/\nu_s} \right) \quad (14)$$

where $V_{Ts}^2 = T_{s0}/m_s$ and $k_\perp$ is the wave number of the vector perpendicular to $\boldsymbol{B}$ and $k_\parallel$ is along $\boldsymbol{B}$.

Table 1
Parameters Used in the Baseline Simulation

Variable	Value	Variable	Value
dx, dy	1.0 mm	nx, dx	1024
dt	1.6 ns	m_n	1.67×10^{-27} kg
T_n	3800 K		
E_0	12.5 V m^{-1}		
No. of Species	5		
Species 0 (electrons)			
n_e	2.5×10^{13} m^{-3}	n_{ev}	5.4×10^8 particles
m_e	9.1×10^{-31} kg	ν_e	1.36×10^7 s^{-1}
Species 1 (H$^+$)			
n_H	1.37×10^{13} m^{-3}	n_{Hv}	2.35×10^9 particles
m_H	1.67×10^{-27} kg	ν_H	1.1×10^6 s^{-1}
Species 2 (Fe$^+$)			
n_{Fe}	1.117×10^{12} m^{-3}	n_{Fev}	3.90×10^8 particles
m_{Fe}	9.34×10^{-26} kg	ν_{Fe}	5.3×10^3 s^{-1}
Species 3 (C$^+$)			
n_C	3.89×10^{12} m^{-3}	n_{Cv}	6.68×10^8 particles
m_C	2.01×10^{-26} kg	ν_C	2.4×10^4 s^{-1}
Species 4 (Avg. Mg$^+$ & Si$^+$)			
n_M	5.25×10^{12} m^{-3}	n_{Mv}	8.90×10^8 particles
m_M	4.4×10^{-26} kg	ν_M	1.1×10^4 s^{-1}

Note. The number of particles refers to PIC particles, each of which represents many actual plasma particles (Birdsall & Langdon 1985).

Assuming strongly magnetized electrons, $\kappa_e \gg 1$, but moderately magnetized ions, $\kappa_j \lesssim 1$, we have

$$B_e = \frac{4}{3\omega_{ke}} \frac{(1 - i\omega_{ke}/\nu_e)(\boldsymbol{k}_\perp \cdot \boldsymbol{V}_0) - e(\boldsymbol{k}_\perp \cdot \boldsymbol{E}_0)/(m_e \nu_e)}{\kappa_e^2 + (1 - i\omega_{ke}/\nu_e)^2} \quad (15)$$

where

$$\boldsymbol{U}_j \equiv \boldsymbol{V}_e - \boldsymbol{V}_j \approx \boldsymbol{V}_0 - \boldsymbol{V}_j = \left(\boldsymbol{V}_0 - \frac{q_j \boldsymbol{E}_0}{m_j \nu_j} \right) \Big/ (1 + \kappa_j^2). \quad (16)$$

Many of these notations were used and explained in an ionospheric context in Dimant & Oppenheim (2004a)

This complex dispersion relationship requires a numerical solution. For the parameters used in the simulation and listed in Table 1, Figure 9 shows the growth rate as a function of wave number. One can see that the peak growth occurs at ∼23 cm. This compares nicely with the peak wavelength of growth in the simulation that we estimated at ∼19 cm. The growth rate of a few times 10^4 per second approximately matches the simulation growth rate. Likewise the angle off the $\boldsymbol{V}_0$ direction predicted by the dispersion relation is roughly 20 degrees. This is a bit less than the simulation and needs further investigation. Overall, this is in good agreement.
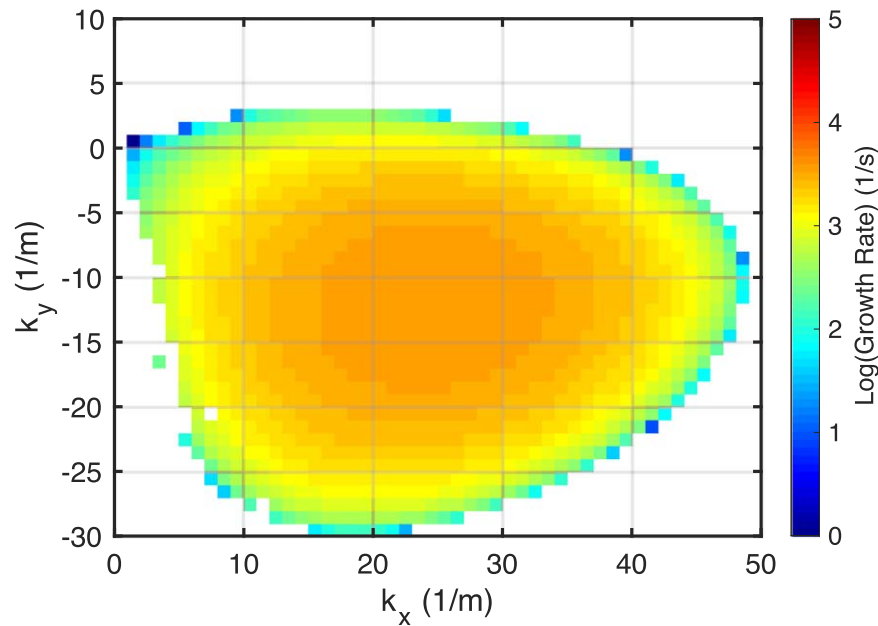
Figure 9. Growth rate as a function of wave number for the parameters in Table 1. Outside of the colored region, the growth rate is negative. The predicted wavelength of maximum growth is ~23 cm ($|k_{max}| = 27$ m^{-1}) and points 26° degrees off the $\boldsymbol{E} \times \boldsymbol{B}$ direction, similar to that seen in the simulation.

ORCID iDs

Meers Oppenheim ⓘ https://orcid.org/0000-0002-8581-6177
Yakov Dimant ⓘ https://orcid.org/0000-0002-3807-5820
William Longley ⓘ https://orcid.org/0000-0002-8518-8633
Alex C. Fletcher ⓘ https://orcid.org/0000-0003-4969-4130

References

Aschwanden, M. J., Tarbell, T. D., Nightingale, R. W., et al. 2000, ApJ, 535, 1047
Athay, R. G. 1966, ApJ, 146, 223
Avrett, E. H., & Loeser, R. 2008, ApJS, 175, 229
Birdsall, C. K., & Langdon, A. B. 1985, Plasma Physics Via Computer Simulation (New York: McGraw-Hill)
Carlsson, M., Hansteen, V. H., Pontieu, B. D., et al. 2007, PASJ, 59, S663
Dalgarno, A., McDowell, M. R. C., & Williams, A. 1958, RSPTA, 250, 411
De Pontieu, B., Rouppe van der Voort, L., McIntosh, S. W., et al. 2014, Sci, 346, 1255732
Dimant, Y. S., & Milikh, G. M. 2003, JGRA, 108, 1350
Dimant, Y. S., & Oppenheim, M. M. 2004a, JASTP, 66, 1655
Dimant, Y. S., & Oppenheim, M. M. 2004b, JASTP, 66, 1639
Dimant, Y. S., Oppenheim, M. M., & Fletcher, A. C. 2016, PhPl, 23, 084503
Dimant, Y. S., & Sudan, R. N. 1995, JGR, 100, 14605
Dimant, Y. S., & Sudan, R. N. 1997, JGR, 102, 2551
Fletcher, A. C., Dimant, Y. S., Oppenheim, M. M., & Fontenla, J. M. 2018, ApJ, 857, 129
Fontenla, J. M. 2005, A&A, 442, 1099
Fontenla, J. M., Avrett, E. H., & Loeser, R. 1993, ApJ, 406, 319
Fontenla, J. M., Curdt, W., Haberreiter, M., Harder, J., & Tian, H. 2009, ApJ, 707, 482
Fontenla, J. M., Peterson, W. K., & Harder, J. 2008, A&A, 480, 839
Fossum, A., & Carlsson, M. 2005, Natur, 435, 919
Foster, J. C., & Erickson, P. J. 2000, GeoRL, 27, 3177
Gogoberidze, G., Voitenko, Y., Poedts, S., & De Keyser, J. 2014, MNRAS, 438, 3568
Gogoberidze, G., Voitenko, Y., Poedts, S., & Goossens, M. 2009, ApJL, 706, L12
Grant, S. D. T., Jess, D. B., Zaqarashvili, T. V., et al. 2018, NatPh, 14, 480
Gudiksen, B. V., Carlsson, M., Hansteen, V. H., et al. 2011, A&A, 531, A154
Gurevich, A. V. 1978, Series on Physics Chemistry Space (Berlin: Springer)
Hotta, H., Iijima, H., & Kusano, K. 2019, SciA, 5, eaau2307
Jeffrey, N. L. S., Fletcher, L., Labrosse, N., & Simões, P. J. A. 2018, SciA, 4, eaav2794
Kagan, L. M., & Kelley, M. C. 2000, JGR, 105, 5291
Liu, J., Nelson, C. J., Snow, B., Wang, Y., & Erdélyi, R. 2019, NatCo, 10, 3504
Liu, J., Wang, W., Oppenheim, M., et al. 2016, GeoRL, 43, 2351
Longley, W. J., Oppenheim, M. M., & Dimant, Y. S. 2019, JGRA, 124, 6313
Madsen, C. A., Dimant, Y. S., Oppenheim, M. M., & Fontenla, J. M. 2014, ApJ, 783, 128
Martínez-Sykora, J., Pontieu, B. D., Carlsson, M., et al. 2017a, ApJ, 847, 36
Martínez-Sykora, J., Pontieu, B. D., & Hansteen, V. 2012, ApJ, 753, 161
Martínez-Sykora, J., Pontieu, B. D., Hansteen, V. H., et al. 2017b, Sci, 356, 1269
Milikh, G. M., & Dimant, Y. S. 2003, JGRA, 108, 1351
Oppenheim, M. M. 1997, AnGeo, 15, 899
Oppenheim, M. M., Dimant, Y., & Dyrud, L. P. 2008, AnGeo, 26, 543
Oppenheim, M. M., & Dimant, Y. S. 2004a, JASTP, 66, 1639
Oppenheim, M. M., & Dimant, Y. S. 2004b, JASTP, 66, 1655
Oppenheim, M. M., & Dimant, Y. S. 2013, JGRA, 118, 1306
Pontieu, B. D., Erdélyi, R., & James, S. P. 2004, Natur, 430, 536
Rubio, L. B., & Suárez, D. O. 2019, LRSP, 16, 1
Schunk, R. W., & Nagy, A. F. 2009, Ionospheres (2nd ed.; Cambridge: Cambridge Univ. Press)
Stein, R. F., & Nordlund, Å. 2006, ApJ, 642, 1246
Vernazza, J. E., Avrett, E. H., & Loeser, R. 1981, ApJS, 45, 635
Vranjes, J., & Krstic, P. S. 2013, A&A, 554, A22